

CCFE–RE(10)09

S.L. Dudarev, M.R. Gilbert,
K. Arakawa, H. Mori, Z. Yao,
M.L. Jenkins, P.M. Derlet

A Langevin model for real-time Brownian dynamics of interacting nano-defects in irradiated metals

Enquiries about copyright and reproduction should in the first instance be addressed to the Culham Publications Officer, Culham Centre for Fusion Energy (CCFE), Library, Culham Science Centre, Abingdon, Oxfordshire, OX14 3DB, UK. CCFE is the fusion research arm of the United Kingdom Atomic Energy Authority, which is the copyright holder.

A Langevin model for real-time Brownian dynamics of interacting nano-defects in irradiated metals

S.L. Dudarev¹, M.R. Gilbert^{1;2}, K. Arakawa^{3;4;5}, H. Mori³, Z. Yao^{2;6}, M.L. Jenkins²,
and P.M. Derlet⁷

CCFE, Culham Science Centre, OX14 3DB, Abingdon, UK

¹*EURATOM/CCFE Fusion Association, Culham Centre for Fusion Energy,
Abingdon, Oxfordshire OX14 3DB, UK.*

²*Department of Materials, University of Oxford, Parks Road, Oxford OX1 3PH, UK.*

³*Research Center for Ultra-High Voltage Electron Microscopy,
Osaka University, 7-1 Mihogaoka, Ibaraki, Osaka 567-0047, Japan.*

⁴*Okinawa Institute of Science and Technology, Kunigami, Okinawa 904-0411, Japan.*

⁵*JST, CREST, 5 Sanbancho, Chiyoda-ku, Tokyo 102-0075, Japan.*

⁶*Department of Mechanical and Materials Engineering, Queen's University,
Nicol Hall, 60 Union Street, Kingston K7L 3N6, Ontario, Canada.*

⁷*Condensed Matter Theory Group, Paul Scherrer Institut, CH-5232 Villigen PSI, Switzerland.*

A Langevin model for real-time Brownian dynamics of interacting nano-defects in irradiated metals.

S.L. Dudarev¹, M.R. Gilbert^{1,2}, K. Arakawa^{3,4,5}, H. Mori³, Z. Yao^{2,6}, M.L. Jenkins², and P.M. Derlet⁷

¹EURATOM/CCFE Fusion Association, Culham Centre for Fusion Energy, Abingdon, Oxfordshire OX14 3DB, UK.

²Department of Materials, University of Oxford, Parks Road, Oxford OX1 3PH, UK.

³Research Center for Ultra-High Voltage Electron Microscopy,
Osaka University, 7-1 Mihogaoka, Ibaraki, Osaka 567-0047, Japan.

⁴Okinawa Institute of Science and Technology, Kunigami, Okinawa 904-0411, Japan.

⁵JST, CREST, 5 Sanbanchō, Chiyoda-ku, Tokyo 102-0075, Japan.

⁶Department of Mechanical and Materials Engineering, Queen's University,
Nicol Hall, 60 Union Street, Kingston K7L 3N6, Ontario, Canada.

⁷Condensed Matter Theory Group, Paul Scherrer Institut, CH-5232 Villigen PSI, Switzerland.

In-situ real-time electron microscope observations of metals irradiated with ultra-high-energy electrons or energetic ions show that the dynamics of microstructural evolution in these materials is strongly influenced by long-range elastic interactions between mobile nano-scale radiation defects. Treating long-range interactions is also necessary for modelling microstructures formed in *ex-situ* high-dose-rate ion-beam irradiation experiments, and for interpolating the ion-beam irradiation data to the low-dose-rate limit characterizing the neutron irradiation environments of fission or fusion power plants. We show that simulations, performed using an algorithm where nano-scale radiation defects are treated as interacting Langevin particles, are able to match and explain the real-time dynamics of nano-defects observed in *in-situ* electron microscope experiments.

PACS numbers: 61.72.-y, 61.80.-x, 61.82.Bg

I. INTRODUCTION

Recent *in-situ* electron microscope observations, providing real-time visualization of dynamics of defects produced by ultra-high-energy electron irradiation¹⁻³, or showing microstructural evolution occurring under ion beam⁴⁻⁶ irradiation, have revolutionized our understanding of how properties of metals and alloys change in the extreme radiation and thermal environments of a fission or a fusion power plant. The key feature of *in-situ* electron microscopy is its ability to exhibit the time-dependent dynamics of migration, interaction, and transformation of radiation defects, and to visualize the entire complexity of evolving defect and dislocation networks. For example, *in-situ* electron microscope observations provided evidence of violation of the Burgers vector conservation law for dislocations on the nano-scale¹. This gave a vital clue needed for modelling microscopic processes responsible for the formation of unusual high-temperature dislocation structures in iron^{7,8}, and for explaining the origin of the loss of strength of ferritic-martensitic steels⁹ at high temperatures exceeding 500°C.

The development of *in-situ* electron microscope techniques was partially stimulated by the application of large-scale molecular dynamics (MD) simulations to modelling mobile defects and clusters of defects (for example nano-dislocation loops) in iron and other metals^{10,11,14-17}. A hypothesis stating that clusters of point defects play a significant part in microstructural evolution of irradiated materials was proposed in the

1990s within the framework of the ‘production bias’ radiation damage model¹⁸. However, it is only recently that *in-situ* electron microscope observations¹⁻⁶ confirmed the fact that mobile and immobile clusters of point defects form an integral part of the microstructure of an irradiated material.

Somewhat surprisingly, interpreting *in-situ* real-time electron microscope observations remains genuinely problematic. The ten orders of magnitude mismatch between the nanosecond (10^{-9} s) timescale accessible to an MD simulation^{10,11,14-17}, and the 10 to 1000 seconds timescale of a typical *in-situ* electron microscope observation¹⁻⁶, impedes meaningful quantitative analysis. The need to develop a model, with which real-time observations could be simulated and interpreted, does not only stem from the fact that electron microscopy *per se* is a highly quantitative technique for characterizing materials^{19,20}. Recently the question about how to model, in real time, the evolution of an ensemble of mobile interacting radiation defects has been brought into focus by the rapidly growing applications of ion-beam sources to simulating neutron irradiation damage effects in fission and fusion materials.

In-situ electron microscope observations visualize the dynamics of microstructure corresponding to the limit of high irradiation dose rates, approaching 10^{-3} dpa·s⁻¹ (~ 80 dpa per 24 hours) for the ultra-high-voltage electron irradiation case¹⁻³, and 6×10^{-4} dpa·s⁻¹ to 8×10^{-4} dpa·s⁻¹ (~ 50 to 70 dpa per 24h) for the *in-situ* ion-beam irradiation case⁴⁻⁶. These dose rates are similar to the 10 dpa per 24h to 100 dpa per 24h range of dose rates characterizing irradiation conditions in *ex-situ* ion-

beam facilities²¹. *In-situ* electron microscopy, and *ex-situ* ion-beam irradiation experiments generate similar microstructures, corresponding to a similar range of high irradiation dose rates. These dose rates are several orders of magnitude higher than the rates associated with the irradiation environment of a fission nuclear reactor²², an accelerator-driven system like the International Fusion Materials Irradiation Facility (IFMIF)²³, or a fusion power plant²⁴.

Is there a fundamental difference between microstructures formed in the limits of low and high dose rates? The density of defects generated by irradiation in a unit volume of the material per unit time is the main quantity distinguishing defect production under intense high-dose-rate ion-beam or ultra-high-voltage-electron irradiation, and under low-dose-rate neutron irradiation. This quantity is much higher for high-energy electron or ion beam irradiation than for neutron irradiation. Since the frequency of interaction events in an ensemble of moving particles is proportional to the square of the density of particles, one should expect that various phenomena associated with the presence of interaction between radiation defects should be more pronounced in the limit of high irradiation dose rate, and should be readily seen in *in-situ* electron microscope experiments. Indeed, there is experimental evidence for the effect of dose rate on microstructural evolution of irradiated materials^{25–27}.

In-situ electron microscope observations show that simultaneous, as opposed to sequential, production of mobile defects at high irradiation dose rates results in microstructural evolution that is influenced by the ‘collective’ dynamical events involving correlated motion of several defects, leading to the formation of defect rafts, coalescence of defects, and the eventual self-organization and spatial ordering of defects. All these phenomena are routinely seen in *in-situ* electron microscope experiments^{1–6}, suggesting that interaction between radiation defects does play a significant part in the dynamics of microstructural evolution in the limit of high irradiation dose rates.

The fact that elastic interactions between defects might affect microstructural evolution of a material under irradiation was noted by Hudson *et al.*^{28,29} who investigated, using kinetic Monte Carlo simulations, the evolution of ensembles of interacting defects. The kinetic Monte Carlo model developed by Hudson *et al.*²⁹ treated the effect of elastic forces through the use of hopping probabilities biased by the spatially-dependent elastic fields. The study showed that while the effect of elastic forces on the evolution of ensembles of one-dimensionally migrating dislocation loops was indeed significant²⁸, in agreement with earlier MD predictions showing that vacancies pin the motion of glissile dislocation loops^{30,31}, the elastic interactions between three-dimensionally migrating defects do not appear to have an appreciable effect on microstructural evolution²⁹. For the treatment of a general case of long-term microstructural evolution, further work is clearly needed to elucidate the role of elastic interactions between the defects. Recent implemen-

tations of accelerated kinetic Monte Carlo algorithms for simulating the accumulation of radiation damage^{32,33} are however based on the assumption that defects perform unbiased (by internal elastic fields) three-dimensional migration in the material, and interactions between defects are described as short-range inelastic ‘collisions’. These simulations do not include the treatment of long-range elastic forces acting between the defects, and between defects and dislocations, and moreover do not take into account the effects of one-dimensional Brownian motion of prismatic dislocation loops often observed experimentally^{1–6}.

In this paper we describe a possible alternative (to kinetic Monte Carlo) approach to simulating the long timescale evolution of radiation-induced microstructures. The development of this approach has been stimulated by the fact that understanding the microscopic mechanisms driving microstructural evolution, and matching simulations to experiment, requires modelling *particular* microscopic realizations of evolving defect structures, like those observed by *in-situ* electron microscopy. Indeed, certain properties of an irradiated material, for example its fracture toughness or thermal conductivity, depend on the statistical characteristics of irradiation-induced microstructure involving many defects and dislocations, and hence represent self-averaging quantities. At the same time, validating a microstructural evolution model requires understanding the dynamics of interaction between radiation defects, and comparing the results of simulations with *local* experimental observations, often involving only a few (e.g. two or three) defects, where no statistical ensemble averaging is possible.

Bearing this in mind, in the approach described below we treat defects as interacting objects satisfying a set of linked Langevin equations of motion. It is known that in terms of ensemble averaged quantities, solutions of linked Langevin equations in the strong friction (overdamped) limit are equivalent to the solutions of a multi-dimensional diffusion equation^{34,35}, and hence they are equivalent to solutions found using kinetic Monte Carlo simulations²⁹. The advantage offered by the Langevin equations-based treatment is that integrating stochastic differential equations for an ensemble of interacting objects is computationally no more difficult than integrating them for an ensemble of non-interacting particles.

There are further obvious computational advantages offered by the similarity between the Langevin and the MD integration algorithms, like the ease of parallelizing the method. Also, by solving the Langevin equations we explicitly follow the trajectories of migrating defects^{36,37} corresponding to the initial conditions defined by experimental observations, whereas kinetic Monte Carlo algorithm^{29,33} operates on the logarithmic timescale, which speeds up calculations but makes it more difficult to compare simulations with observations. Hence, the modes of microstructural evolution predicted by the Langevin dynamics model can be matched and verified explicitly against real-time *in-situ* electron mi-

croscopy experiments. Furthermore, the speed of the integration algorithm for Langevin dynamics is entirely independent of whether the defects migrate three- or one-dimensionally. One can easily apply the method to the treatment of either limit, with the potential for generalization to modeling reactions between the defects and between dislocations and the defects.

The paper is organized as follows. We start from giving a brief summary of *in-situ* electron microscope observations, which show evidence of the significant part played by the interaction between mobile radiation effects. We then introduce the simulation method, describe how to treat long-range interactions between defects (the ‘Langevin particles’), and compare the simulated trajectories of defects with experimental observations. Finally, we discuss effects of interaction between mobile radiation defects and pinning centres (for example vacancy clusters), and show that the presence of pinning centres explains the unusual trajectories of migration of defects observed in *in-situ* electron microscope experiments on ion-irradiated materials^{4–6}.

II. BROWNIAN MOTION OF INTERACTING NANO-DISLOCATION LOOPS: *IN-SITU* ELECTRON MICROSCOPE OBSERVATIONS

In-situ electron microscope observations show two distinctly different modes of microstructural evolution, and two different types of defect dynamics, the occurrence of which depends on the type of particles irradiating the material. The ultra-high-energy electron irradiation^{1–3} produces individual Frenkel pairs of vacancies and self-interstitial atoms, and the resulting supersaturation of defects gives rise to the nucleation and growth of small self-interstitial dislocation loops and vacancy clusters. Ion-beam irradiation^{4–6} generates collision cascades, in which self-interstitial and vacancy defects form clusters as cascades cool down and re-solidify^{11,18,38}.

In the case of ultra-high-energy electron irradiation, 99.998 wt.% pure bcc Fe (the metal most extensively studied by *in-situ* microscopy so far) was used for making specimens. The impurity content characterizing the specimens is fully described in the supporting on-line material for Ref.². The specimens were rolled into 0.08mm-thick sheets, which were pre-annealed at 1073K for 2 hours in a hydrogen atmosphere, and electrochemically polished. The orientation of the specimen surfaces was set close to $(1\bar{1}0)$ to minimize the image force acting on loops whose Burgers vectors \mathbf{b} , defining the directions in which the loops migrate, were $1/2[111]$ or $1/2[11\bar{1}]$. High-energy electron irradiation was performed in an ultra-high-voltage electron microscope H-3000(Hitachi) operated at an acceleration voltage of 2000 kV. The dynamics of formation and migration of small dislocation loops was observed under electron irradiation. In another set of experiments, the dynamics of thermal Brownian motion of nano-scale dislocation loops initially produced by

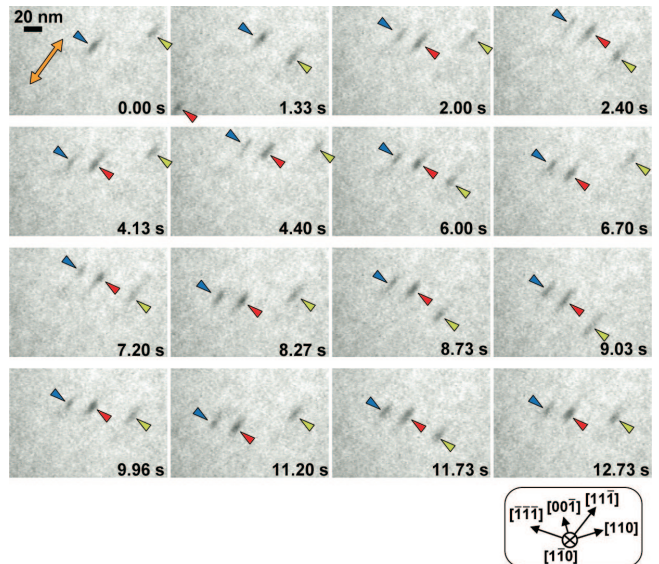


FIG. 1: A sequence of *in-situ* electron microscope snapshots recorded for $\mathbf{g} = 002$ diffraction conditions at a 200 kV accelerating voltage, and showing the evolution of an ensemble of three prismatic $a/2[11\bar{1}]$ dislocation loops formed in nominally pure iron by ultra-high voltage electron irradiation prior to the *in-situ* experiment. The loops perform one-dimensional Brownian motion in the direction parallel to their Burgers vector at $T = 673\text{K}$. The loop diameters, from left to right, are 6nm, 6.5nm, and 6nm. The projected separation between the glide cylinders for the loops on the left (L) and in the centre (C) is 23nm, and the projected separation between the glide cylinders for the loops in the centre (C) and on the right (R), is 41nm.

electron irradiation was observed using sample heating in an analytical H-800 (Hitachi) microscope operated at a relatively low acceleration voltage of 200 kV, at which no further radiation damage is produced. We note here that observing the migration of dislocation loops in an electron microscope inevitably gives rise to the electron beam itself affecting the observed mobility of the loops^{12,13}. This electron beam effect does not significantly affect experimental observations described in this paper, making it possible to attribute the observed mobility of dislocation loops to thermal activation.

Specimen heating was performed following ultra-high-energy electron irradiation at temperatures ranging from 110K to 200K. The specimens were heated to temperatures in the range between 290K and 850K. Bright-field imaging was used for areas of the specimen where thickness varied between 100nm to 300nm. The observation axis was approximately $[1\bar{1}0]$ for diffraction \mathbf{g} -vectors 110 and 002, with the deviation parameter from the exact Bragg condition s ranging from 0.02 to 0.06 nm^{-1} . Images were recorded using a silicon intensifier target camera with the time resolution of 1/30 s. It was possible to observe dislocation loops with diameters greater than a few nanometers.

In-situ electron microscope observations show that the

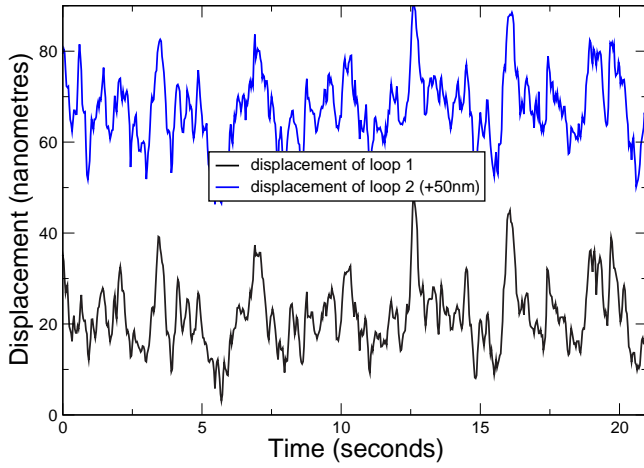


FIG. 2: Trajectories of motion for two interacting $d = 16\text{nm}$ and $d = 15\text{nm}$ prismatic $a/2\langle 111 \rangle$ dislocation loops migrating in pure iron foil at $T = 650\text{K}$. The thickness of the foil is approximately 250nm and the glide cylinders of the loops are 37nm apart, as measured using stereo microscopy. The loops were formed by ultra-high energy electron irradiation followed by specimen annealing.

dynamics of motion of loops is *visibly* affected by elastic interactions between the loops. For example, Figure 1 shows that three mobile prismatic dislocation loops formed in pure iron under ultra-high voltage electron irradiation, and initially separated by large distances, perform Brownian motion along their glide cylinders, and eventually approach each other closely enough so that the dynamics of loops becomes correlated due to elastic interaction between the loops. The loops eventually form a raft that migrates as a single entity, then grows and gradually coalesces into a single loop.

Other examples found by *in-situ* electron microscope examination of specimens irradiated by ultra-high-energy electrons show processes of capture of a mobile loop by the elastic field of another loop, followed by the coalescence of the loops. In general, the trend seen in *in-situ* electron microscope observations of defects migrating in high purity iron, and illustrated in Figure 2, is that the motion of the defects is highly correlated, and the typical Brownian trajectories of defects follow each other on a $\sim 0.1\text{ s}$ timescale.

For ion-beam irradiation experiments, we used high purity Fe (containing $\sim 1\text{ ppm}$ carbon, $< 5\text{ ppm}$ nitrogen, $< 10\text{ ppm}$ silicon, and very small quantities of other impurities, which is not dissimilar to the impurity content of the specimens used for ultra-high-energy electron irradiation experiments). The cold-rolled as-received material was annealed in vacuum at 1073K for an hour followed by slow cooling. After this treatment all specimens had a simple ferritic microstructure with a low dislocation density. Thin foils were prepared by electropolishing and irradiated with 100 or 150 keV Fe^+ and Xe^+ ions at room temperature (RT), and at 573K and 773K in the Argonne IVEM-Tandem Facility³⁹. The microscope was

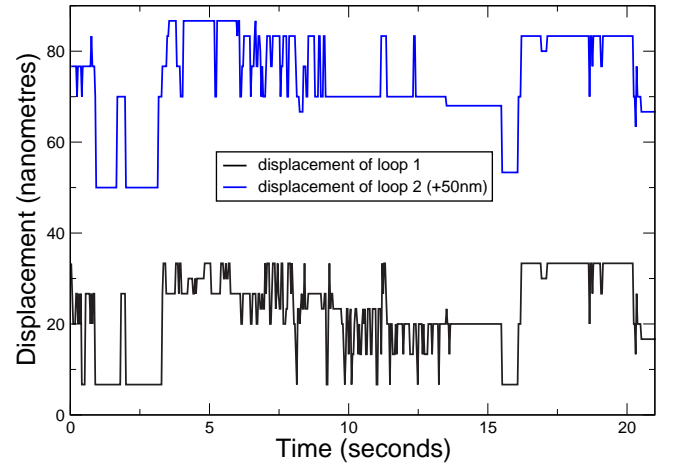


FIG. 3: Experimentally observed trajectories of migration for two prismatic $\mathbf{b} = a/2[111]$ dislocation loops, both of similar size $d \approx 4\text{nm}$, performing thermally activated Brownian motion in pure iron after the specimen was irradiated with 150 keV Fe^+ ions to a dose of $\sim 0.65\text{ dpa}$. The projected distance between the glide cylinders of the loops is 12nm . The temperature of the specimen is 673K . Note the significant degree of correlation between the trajectories of motion of the loops shown in this figure.

operated at 200 keV , below the threshold for knock-on radiation damage in Fe. Dynamic observations followed the evolution of damage over doses up to 13 dpa , according to a SRIM calculation with a displacement energy of 24 eV . Irradiations were paused from time to time to allow detailed characterization of microstructures using a number of diffraction-contrast techniques⁴⁻⁶. Similar detailed characterization was performed at the end of the irradiation, after the specimens irradiated at elevated temperatures had cooled to room temperature.

The pattern of migration of nano-dislocation loops in *ion*-irradiated UHP iron is surprisingly different from that of loops migrating in UHP iron irradiated with ultra-high-energy electrons (see Figure 2). This fact was highlighted in Ref.⁴⁰ (see Figure 3 of Ref.⁴⁰, which shows how different are the observed and simulated trajectories of defect migration), and was noted in Refs.^{4,6}.

Figure 3 shows trajectories of migration for two nano-dislocation loops in ion-irradiated iron. The trajectories exhibit a significant degree of correlation, similarly to the case of three migrating loops illustrated in Figure 1. However, as opposed to the case of electron-irradiated iron, the trajectories of loops migrating in ion-irradiated iron do not look like the characteristic ‘fractal’ Brownian trajectories shown in Figure 2 and predicted by MD simulations^{17,37}. The trajectories showed in Figure 3 demonstrate that the motion of loops consists of a series of relatively infrequent long-range ‘instantaneous’ jumps, separated by extended intervals of time, during which the loops are pinned at certain points in the specimen and remain effectively immobile. Here we draw the attention of the reader again to the large difference between

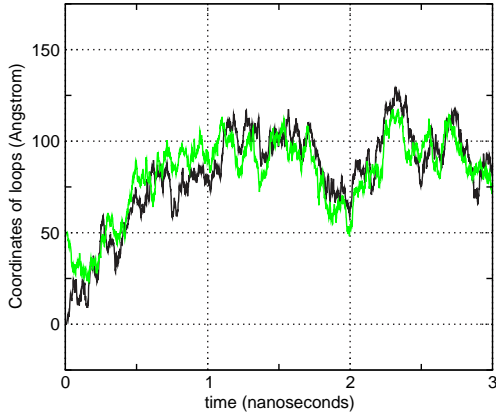


FIG. 4: Trajectories of motion, simulated using molecular dynamics, for two interacting $\mathbf{b} = a/2[111]$ 61-atom ($d \approx 1.8\text{nm}$) prismatic dislocation loops migrating in iron at $T = 500\text{K}$. The centres of loops are separated in the $[1\bar{1}0]$ direction by the distance $l \approx 40.5\text{\AA}$.

the timescales characterizing experimental observations ($\sim 20\text{ s}$ for the examples shown in Figs. 2 and 3) and MD simulations ($\sim 10^{-9}\text{ s}$ for the cases investigated in Refs.^{17,37}).

In subsequent sections of the paper we show that the occurrence of correlated motion of loops, and the unusual shape of the trajectories of loops observed in experiments on ion-irradiated materials, can be explained if we assume that individual loops interact with other loops, and that they also interact with the ‘invisible’ elements of microstructure, for example small vacancy clusters formed in collision cascades generated by ion irradiation⁴¹.

We first investigate effects of migration of interacting loops using MD simulations, and then generalize the treatment to the case of Langevin dynamics of interacting defects. Using the latter method, we are able to match the timescales of experimental observations and simulations over intervals of time many orders of magnitude longer than those accessible to MD simulations. By assuming that loops interact *via* long-range elastic forces, we simulate the trajectories of correlated Brownian motion of the loops, and show that those also match experimental observations. Finally, using the isotropic elasticity expressions for the energy of interaction between the self-interstitial atom loops and vacancy clusters, we are able to simulate the unusual ‘pinned’ Brownian trajectories of loops found experimentally in ion-irradiated iron and shown in Figure 3.

III. A MOLECULAR DYNAMICS MODEL FOR INTERACTING NANO-DISLOCATION LOOPS.

We start our analysis with an MD investigation of how two small prismatic dislocation loops migrate if the glide cylinders of the loops are in close proximity to each other. Simulations were performed using the re-

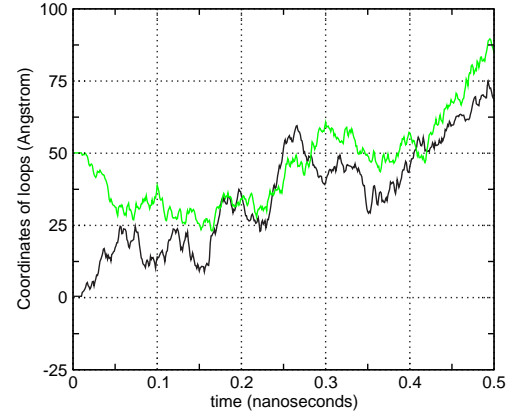


FIG. 5: Trajectories of motion for interacting loops simulated using molecular dynamics and shown in Figure 4 but plotted for a shorter interval of time. Initially the loops are 5nm apart in the direction of their Burgers vector. Elastic interaction brings the loops together at $t \approx 0.17\text{ns}$. After this moment Brownian motion of the two loops becomes strongly correlated, the loops form a raft and migrate almost as a single entity.

cent ‘magnetic’ interatomic potential⁴² for $\alpha\text{-Fe}$. Two 61-SIA (self interstitial atom) $\frac{1}{2}\langle 111 \rangle$ dislocation loops were inserted into a regular $30 \times 20 \times 60$ cell (in the $(x, y, z) = ([1\bar{1}0], [11\bar{2}], [111])$ coordinate system) containing 216000 atoms with periodic boundary conditions in all coordinate directions. These two 18.7 \AA diameter loops were inserted with their centres separated by $l \approx 40.5\text{ \AA}$ in the $[1\bar{1}0]$ direction, but with the same position ($y_1 - y_2 \approx 0$) along the $[11\bar{2}]$ direction. This $[1\bar{1}0]$ separation is comparable with the size of the loops themselves, but is still large enough to ensure that there is no overlap between the core regions of the edge dislocations forming the loops, so that all the interaction effects found in simulations are attributable to the long-range elastic fields of the loops. Note that this $\sim 4\text{ nm}$ interaction distance in $x = [1\bar{1}0]$ is smaller than the separation between the loops through the x -direction periodic boundary ($\approx 8\text{ nm}$), which means that the ‘internal’ 4 nm elastic interactions dominate. Each loop was given a random initial position along its respective $z = [111]$ glide cylinder.

After relaxing (quenching to 0K) the simulation cell, a sequence of 5 ps finite temperature simulations were performed at 100K intervals to bring the system up to the 500K temperature corresponding to the result presented here. The evolution of the two-loop system was simulated for a 3 ns interval at 500K , during which the positions of the loops were measured every 1 ps . The resulting 1-dimensional $[111]$ trajectories of the loops generated during this simulation are shown in Figures 4 and 5. Following a method similar to that described in^{36,37}, we calculate separate diffusion coefficients D for the motion of the loops, and find a value of approximately $5 \times 10^9\text{ nm}^2\text{s}^{-1}$ for both loops.

There are two aspects of MD simulations described

here that are difficult to relate to experimental observations (see Figures 1 and 3). The difference between the timescales of MD simulations and experimental observations is of the order of 10^9 . Also, the diffusion coefficients for the loops derived from MD simulations are many orders of magnitude larger than those found experimentally². Hence, we do not attempt to directly compare MD simulations and experimental observations, and instead focus on the qualitative aspects of simulations that offer some insight into the origin of the effects observed experimentally.

The most notable feature seen in the simulations is the correlated nature of the migration of the loops. Figures 4 and 5 show that although initially the loops were separated, in the direction parallel to their Burgers vector (which is the direction of one-dimensional Brownian motion of the loops), by a distance of approximately 5nm, after just 170ps the random Brownian motion of the loops became strongly correlated (see Figure 5), and the trajectories of the loops during the rest of the time interval spanned by the simulation closely followed each other. The strongly correlated nature of Brownian motion of the loops found in MD simulations may appear exaggerated in comparison with experimental observations, where loops would occasionally drift apart and separate. However we note that the distance between the glide cylinders set up in MD simulations is almost an order of magnitude smaller in comparison with the distances between the glide cylinders for the loops seen in Figure 1, and hence the strength of elastic interaction between the loops in the MD simulations is much larger than in observations illustrated in Figure 1.

The main conclusion that we derive from these simulations, which illustrate the effect of interaction between the loops on their Brownian motion, is the emergence of a ‘collective’ mode of motion, where trajectories of migration of loops, while exhibiting a considerable degree of randomness, follow each other over an extended period of time. We now show how this conclusion can be generalized and extended to the case of many interacting loops and much longer timescales through the use of the Langevin treatment of dynamics of loops.

IV. RANDOM THERMAL FORCE ACTING ON A DISLOCATION LOOP

The fact that migration of individual self-interstitial crowdion defects and small dislocation loops could be rationalized using a Langevin equation-based treatment was discussed in Refs.^{12,36,37,43}. In this section we prove, using the multi-string Frenkel-Kontorova model⁴⁴, that the centre of mass of a loop moves under the action of random thermal force resulting from thermal vibrations of atoms at the perimeter of the loop, or, in other words, that a small dislocation loop can be treated as a particle, the coordinate of which satisfies the Langevin equation of motion. Figure 6 shows the structure of a 37-self-

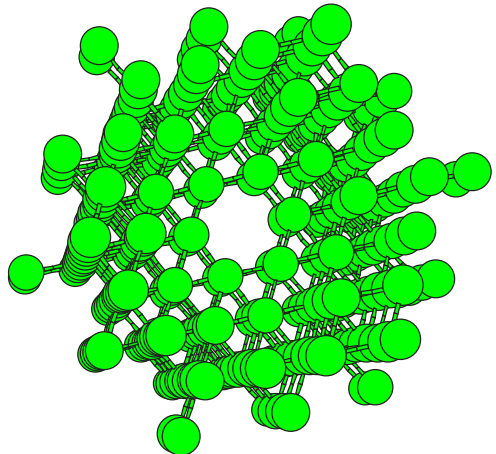


FIG. 6: The equilibrium structure of a small dislocation loop formed by the agglomeration of 37 self-interstitial atoms on a $\langle 111 \rangle$ habit plane in bcc iron^{41,46}. The Burgers vector of the loop is $\mathbf{b} = a/2[111]$, where a is the lattice constant. Only those atoms are shown, the potential energy of which exceeds by 0.05 eV the potential energy of an atom in a perfect lattice. The viewing direction is slightly off the $\langle 111 \rangle$ axis, which is parallel to the Burgers vector of the loop.

interstitial-atom dislocation loop formed in bcc iron by the agglomeration of self-interstitial atoms on the $\langle 111 \rangle$ habit plane. The Burgers vector of the loop, the direction of which is parallel to the atomic strings shown in Figure 6, is $\mathbf{b} = a/2[111]$. Each atomic string, depending on its position in the loop, is described by the profile of atomic displacements in the direction parallel to the Burgers vector $\mathcal{U}_{\mathbf{j}}(n - \mathbf{Z}_{\mathbf{j}}(t)/b)$, where n is the index of an atom in a string, and \mathbf{j} is the two-dimensional index of a string in the plane normal to the plane of the loop^{36,44}. $\mathbf{Z}_{\mathbf{j}}(t)$ is the time-dependent position of the centre of the \mathbf{j} -th atomic displacement profile, which in the case of a single self-interstitial atom defect (a crowdion) can be identified with the position of the defect in the crystal lattice.

By following the method described in Refs.^{12,36,37}, we find a set of coupled equations of motion for the coordinates of centres of displacement profiles associated with atomic strings running in a $\langle 111 \rangle$ -type direction:

$$m \frac{d^2 \mathbf{Z}_{\mathbf{j}}(t)}{dt^2} = 4m\omega^2 \sum_{n, \mathbf{h}} [\Phi_{n, \mathbf{j}}(t) - \Phi_{n, \mathbf{j}+\mathbf{h}}(t)] \times \sin^2 \left\{ \frac{\pi}{a} (\mathcal{U}_{\mathbf{j}}[n - \mathbf{Z}_{\mathbf{j}}(t)/a] - \mathcal{U}_{\mathbf{j}+\mathbf{h}}[n - \mathbf{Z}_{\mathbf{j}+\mathbf{h}}(t)/a]) \right\}. \quad (1)$$

Here $\Phi_{\mathbf{j}, n}(t)$ denotes the field of random (thermal) displacements of atoms in the strings, as opposed to the regular field of time-dependent coordinate $\mathbf{Z}_{\mathbf{j}}(t)$, which

describes migration of the centre of an atomic displacement profile as a whole. The number of equations in the set (1) equals the number of interstitial atoms in the loop. The strings forming the lattice surrounding the loop are assumed to be unaffected by the elastic field of the loop (in other words, for the strings surrounding the loop, $\mathcal{Z}_{\mathbf{j}}(t) = 0$). However, atoms in the lattice surrounding the loop still undergo random thermal motion and interact with atoms in the strings on the perimeter of the loop.

The position of the centre of mass of the loop is given by

$$\mathcal{Z}(t) = \frac{1}{N_s} \sum_{\mathbf{j}} \mathcal{Z}_{\mathbf{j}}(t), \quad (2)$$

where N_s is the number of atomic strings in the loop (for example, for the case shown in Figure 6, $N_s = 37$). Performing the summation over all the strings \mathbf{j} forming the loop, and noting that random forces acting on the neighbouring strings enter the sum with opposite signs, and hence fully compensate each other, we find that the equation of motion for the centre of mass of a loop only contains terms describing thermal forces acting on strings situated at the perimeter of the loop,

$$m \frac{d^2 \mathcal{Z}(t)}{dt^2} = 4m\omega^2 \sum_{n, \mathbf{P}} \sum_{\mathbf{h}'} [\Phi_{n, \mathbf{P}}(t) - \Phi_{n, \mathbf{P}+\mathbf{h}'}(t)] \times \sin^2 \left\{ \frac{\pi}{a} \mathcal{U}_{\mathbf{P}}[n - \mathcal{Z}_{\mathbf{P}}(t)/a] \right\}. \quad (3)$$

Here the summation over \mathbf{P} is performed over strings situated at the perimeter of the loop, where fluctuating phonon forces are not compensated, and summation over \mathbf{h}' is performed over strings in the lattice around the dislocation loop. The right-hand side of equation (3) equals the projection (on the direction of the Burgers vector of the loop) of the total time-dependent random phonon force $f(t)$ acting on the loop. It is known that a random force acting on a particle results in the particle performing Brownian motion. At the same time, according to the fluctuation-dissipation theorem, the presence of randomly fluctuating forces give rise to thermal friction⁴⁵.

Applying the Einstein model for thermal vibrations of atoms to equation (3)³⁶, we find that the correlation function of random force acting on a loop is proportional to the length L of the perimeter of the loop

$$\overline{f(t)f(t')} = f^2 \delta(t - t') \sim L \delta(t - t'). \quad (4)$$

Using the fluctuation-dissipation theorem, we find the coefficient of thermal friction for the loop³⁶

$$\gamma = \frac{f^2}{2k_B T}. \quad (5)$$

The diffusion coefficient D is related to the friction coefficient γ via $D = k_B T / \gamma$. This equation shows that the

diffusion coefficient for a loop treated as a function of its size varies approximately as

$$D \sim L^{-1}, \quad (6)$$

where L is the perimeter of the loop. In what follows, we use this relation to evaluate the diffusion coefficients for loops of various sizes by extrapolating the experimentally measured values for diffusion coefficients found for a loop of a certain size^{2,3}. We note that the dependence of the diffusion coefficient for the centre of mass of the loop on the length of the perimeter of the loop predicted by the Frenkel-Kontorova model described above agrees well with results of MD simulations¹⁷, where it was found that the diffusion coefficient depends on the total number of self-interstitial atoms forming the loop N_s as $D \sim N_s^{-0.64}$, which is close to $D \sim N_s^{-1/2}$ expected from equation (6) in the limit of large loop size. Experimental observations are also broadly in agreement with the above $D \sim L^{-1}$ law^{2,3}.

We note that even in a pure material the diffusion coefficient for a loop is strongly influenced by the presence of impurities, which form a mobile ‘cloud’ around the loop. The presence of this mobile atmosphere of impurities renormalizes the mobility a loop, strongly increasing the effective activation energy for migration in comparison with the estimates derived from MD simulations^{2,3}.

V. A LANGEVIN DYNAMICS MODEL FOR BROWNIAN MOTION OF INTERACTING NANO-DISLOCATION LOOPS

In the previous section we showed that the centre of mass of a dislocation loop moves under the action of an effective random force associated with the thermal motion of atoms in the material. This effective fluctuating thermal force induces stochastic Brownian motion of loops observed in *in-situ* electron microscope experiments¹⁻⁶ and in MD simulations^{10,11,14-17}. Similarly, two nano-dislocation loops formed in close proximity of each other, and interacting *via* long-range elastic forces, perform correlated Brownian motion, as illustrated in Figure 4 and Figure 5.

The diffusion equation for a system of N interacting particles has the form⁴⁷

$$\frac{\partial P}{\partial t} = \sum_{i=1}^N D_i^{\alpha\beta} \left(\frac{\partial^2 P}{\partial r_i^\alpha \partial r_i^\beta} + \frac{1}{k_B T} \left[\frac{\partial U}{\partial r_i^\alpha} \right] \left[\frac{\partial P}{\partial r_i^\beta} \right] \right), \quad (7)$$

where $\alpha, \beta = (x, y, z)$, $P = P(\mathbf{r}_1, \mathbf{r}_2, \dots, \mathbf{r}_N)$ is a N -dimensional probability distribution function, $D_i^{\alpha\beta}$ is the diffusion matrix for particle i , and T is the absolute temperature. The function $U = U(\mathbf{r}_1, \mathbf{r}_2, \dots, \mathbf{r}_N)$ describes the interaction between the particles, and the gradient of this function $F_i^\alpha = -\partial U / \partial r_i^\alpha$ gives the α component of the force acting on particle i .

In the limit of strongly anisotropic one-dimensional diffusion, describing random thermal glide of glissile nano-dislocation loops, equation (7) can be simplified as

$$\frac{\partial P}{\partial t} = \sum_{i=1}^N D_i \left(\frac{\partial^2 P}{\partial z_i^2} + \frac{1}{k_B T} \left[\frac{\partial U}{\partial z_i} \right] \left[\frac{\partial P}{\partial z_i} \right] \right). \quad (8)$$

Here D_i is the diffusion coefficient for loop i , and z_i is the projection of the centre of mass of the loop on the direction of its Brownian motion. We assume that all the loops have the same Burgers vector, which defines the orientation of the glide cylinders and the direction of Brownian motion for the loops.

Equation (8) describes a relatively simple model for an ensemble of interacting Brownian particles, which is even simpler than models considered previously in the context of Brownian dynamics of particles suspended in a fluid and interacting *via* hydrodynamic forces^{48,49}. In principle, the evolution of this model could be investigated using kinetic Monte Carlo simulations, following the method developed by Hudson *et al.*²⁹ who introduced hopping probabilities biased by long-range elastic fields. However, since implementing this approach requires synchronizing the Monte Carlo events, which presents a potentially difficult issue for parallelizing the kinetic Monte Carlo algorithm³³, here we adopt a different strategy and instead focus on a set of differential equations for the coordinates of the loops. To achieve this, we map equation (8) onto a set of N coupled overdamped Langevin equations of the form

$$\frac{dz_i}{dt} = -\frac{D_i}{k_B T} \frac{\partial U}{\partial z_i} + \sqrt{2D_i} \xi_i(t), \quad i = 1, 2, \dots, N. \quad (9)$$

where $\xi_i(t)$ are random variables satisfying the condition $\xi_i(t)\xi_i(t') = \delta(t-t')$, and $U(z_1, z_2, \dots, z_N)$ is the energy of interaction between the loops. The energy of interaction between the loops is, of course, also a function of the position of the loops in the (x, y) plane. However, since the loops do not change their x and y coordinates, we omit explicit reference to these degrees of freedom.

The mathematical equivalence between the overdamped Langevin equations (9) and the many-body diffusion equation (8) exists independently of the microscopic nature of processes responsible for the diffusion of loops^{50,51}, since the only parameters entering both equations are the diffusion coefficients D_i for the particles. Hence statistical simulations of trajectories of loops by means of the Langevin equations (9) are fully equivalent to finding a time-dependent ensemble-averaged solution of a many-body diffusion equation (8). The significant advantage offered by the Langevin equation simulation approach is that by solving these equations we could follow the trajectories of the defects, and compare them with the trajectories observed by *in-situ* electron microscopy. This contrasts with the solutions of the many-body diffusion equation, which describe the evolving microstructure in the statistical ensemble sense. For example, solutions of a many-body diffusion equation cannot

be directly compared with the trajectories of migrating loops observed in *in-situ* experiments.

A. Interaction between an interstitial loop and a vacancy cluster

To investigate the role played by the long-range interaction between an interstitial loop and an immobile pinning centre (a vacancy cluster or an impurity), we use expressions derived from the theory of elasticity. In the isotropic approximation of the theory of elasticity the energy of interaction between a loop and a spherical inclusion is⁵²

$$U(z) = \frac{\Delta V}{3\pi} b\mu \frac{1+\nu}{1-\nu} \frac{1}{\sqrt{z^2 + (R+r)^2}} \times \left[\frac{R^2 - r^2 - z^2}{(R-r)^2 + z^2} E \left(\sqrt{\frac{4rR}{z^2 + (R+r)^2}} \right) + K \left(\sqrt{\frac{4rR}{z^2 + (R+r)^2}} \right) \right]. \quad (10)$$

Here R is the radius of the loop, functions $K(k)$ and $E(k)$ are, respectively, the complete elliptic integrals of the first and second kind, and r and z are the cylindrical coordinates, the origin of which corresponds to the centre of the dislocation loop. ΔV is the relaxation volume (a quantity which has negative sign in the case of a vacancy or a vacancy cluster), \mathbf{b} is the Burgers vector of the loop, $b = |\mathbf{b}|$, and μ and ν are the shear modulus of the material and the Poisson ratio.

Although in principle equation (10) applies equally to an interstitial and a vacancy loop (where in the latter case the energy of interaction has the opposite sign), the fact that a vacancy loop is a metastable configuration that has higher energy than a spherical vacancy cluster (a void)⁴⁶ leads to interstitial loops dominating the observed microstructure of an irradiated material⁶. In what follows we only consider the case of an interstitial dislocation loop that is attracted to a vacancy cluster situated at the axis of the glide cylinder for the loop. In the limit of large separation between the loop and the inclusion $r \gg R$, $z \gg R$, functions $K(k)$ and $E(k)$ can be expanded in the Taylor series as (note that the definition of the argument of these functions differs from that given in Abramovitz and Stegun's handbook⁵³)

$$K(k) \approx \frac{\pi}{2} \left(1 + \frac{k^2}{4} + \frac{9k^4}{64} - \dots \right) \\ E(k) \approx \frac{\pi}{2} \left(1 - \frac{k^2}{4} - \frac{3k^4}{64} - \dots \right), \quad (11)$$

resulting in the far field form of equation (10):

$$U(z) = -\frac{\Delta V}{6} b\mu \frac{1+\nu}{1-\nu} R^2 \frac{1 - 3\cos^2 \theta}{l^3}, \quad (12)$$

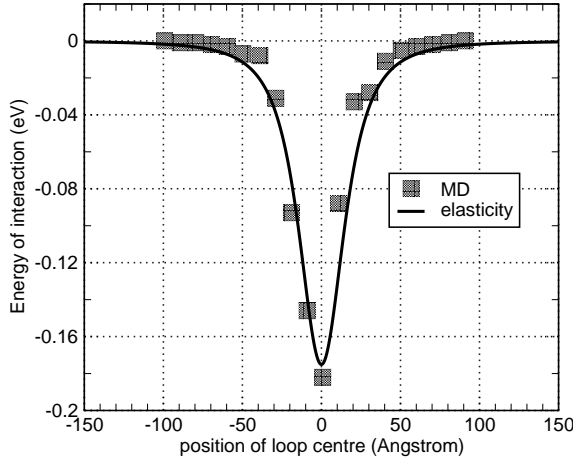


FIG. 7: Energy of interaction between a 313-atom ($R = 2.2\text{nm}$) self-interstitial $\mathbf{b} = a/2\langle 111 \rangle$ dislocation loop and vacancy shown as a function of separation z between the centre of the loop and the vacancy. The vacancy is situated at the axis of the glide cylinder $r = 0$. The solid line follows equation (10) for $\Delta V = -5\text{\AA}^3$, $\nu = 0.29$ and $\mu = 82 \cdot 10^9$ Pa.

where $z/l = \cos \theta$, $r/l = \sin \theta$, and $l = \sqrt{r^2 + z^2}$.

Equation (10) acquires a particularly simple form for $r = 0$, corresponding to the case where the inclusion is situated at the axis of the glide cylinder for the loop

$$U(z) = \frac{\Delta V}{3\pi} \mu \frac{1+\nu}{1-\nu} \frac{\pi R^2 b}{(z^2 + R^2)^{3/2}}. \quad (13)$$

This equation shows that the range of the force field describing elastic interaction between a dislocation loop and an inclusion is of the same order of magnitude as the loop radius R .

Figures 7 and 8 show examples of the potential energy curves describing elastic interactions between a dislocation loop and a single vacancy, or a vacancy cluster. The discrete points are evaluated using atomistic total energy conjugate gradient minimization for a 313-self-interstitial atom loop interacting with a single vacancy situated at the centre of the glide cylinder, or a 10-vacancy cluster situated at the centre of the glide cylinder. The solid curves were calculated using equation (10) and isotropic elastic parameters for pure iron. The effective formation volumes ΔV for a single vacancy and a vacancy cluster were chosen to fit the MD simulation data. These values are broadly in agreement with the literature data on formation volumes of vacancy defects^{54,55}, which themselves are subject to considerable uncertainty and fluctuations. We see that, depending on the formation volume of a vacancy defect, the magnitude of interaction between a self-interstitial loop and a vacancy defect $U(z)$ varies between 0.2 eV and 1 eV. The width of the potential wells shown in Figures 7 and 8 are comparable with the diameter of the dislocation loop.

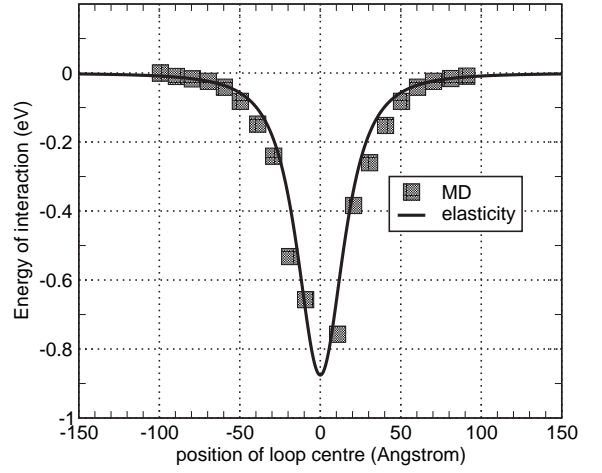


FIG. 8: Energy of interaction between a 313-atom ($R = 2.2\text{nm}$) self-interstitial $\mathbf{b} = a/2\langle 111 \rangle$ dislocation loop and a 10 vacancy-cluster shown as a function of separation z between the centre of the loop and the cluster. The vacancy cluster is situated at the axis of the glide cylinder $r = 0$. The solid line follows equation (10) for $\Delta V = -25\text{\AA}^3$, $\nu = 0.29$ and $\mu = 82 \cdot 10^9$ Pa.

B. Interaction between two dislocation loops

The energy of interaction between two circular dislocation loops with parallel Burgers vectors \mathbf{b}_1 and \mathbf{b}_2 is given by (see equation (4-40) of Hirth and Lothe⁵⁶)

$$U = \frac{\mu b_1 b_2}{4\pi(1-\nu)} \int_0^{2\pi} d\phi_1 \int_0^{2\pi} d\phi_2 \left[\frac{(\boldsymbol{\rho}(\phi_1) \cdot \boldsymbol{\rho}(\phi_2))}{r} - \frac{(\mathbf{r} \cdot \boldsymbol{\rho}(\phi_1))(\mathbf{r} \cdot \boldsymbol{\rho}(\phi_2))}{r^3} \right]. \quad (14)$$

Here $\mathbf{r} = \mathbf{l} + \boldsymbol{\rho}(\phi_1) - \boldsymbol{\rho}(\phi_2)$ is a vector connecting points situated on the perimeter of the two loops, as shown in Figure 9, and $\boldsymbol{\rho}(\phi_1)$ and $\boldsymbol{\rho}(\phi_2)$ are two radial vectors in the habit planes of the loops.

In the far field region, where $|\boldsymbol{\rho}(\phi_1) - \boldsymbol{\rho}(\phi_2)| \ll |\mathbf{l}|$, we find

$$\frac{1}{r^3} = \frac{1}{|\mathbf{l} + \boldsymbol{\rho}|^3} = \frac{1}{l^3} - \frac{3(\boldsymbol{\rho} \cdot \mathbf{l})}{l^5} + \frac{3\rho^2}{2l^5} + \frac{15(\boldsymbol{\rho} \cdot \mathbf{l})}{2l^7} + \dots, \quad (15)$$

where $\boldsymbol{\rho} = \boldsymbol{\rho}(\phi_1) - \boldsymbol{\rho}(\phi_2)$, and the equation for the energy acquires the form

$$U = \frac{\mu b_1 b_2}{4\pi(1-\nu)} \int_0^{2\pi} d\phi_1 \int_0^{2\pi} d\phi_2 \left[(l^2 + 2\mathbf{l} \cdot \boldsymbol{\rho} + \rho^2)(\boldsymbol{\rho}_1 \cdot \boldsymbol{\rho}_2) - ([\mathbf{l} + \boldsymbol{\rho}] \cdot \boldsymbol{\rho}_1)([\mathbf{l} + \boldsymbol{\rho}] \cdot \boldsymbol{\rho}_2) \right] \times \left[\frac{1}{l^3} - \frac{3(\boldsymbol{\rho} \cdot \mathbf{l})}{l^5} + \frac{3\rho^2}{2l^5} + \frac{15(\boldsymbol{\rho} \cdot \mathbf{l})}{2l^7} + \dots \right]. \quad (16)$$

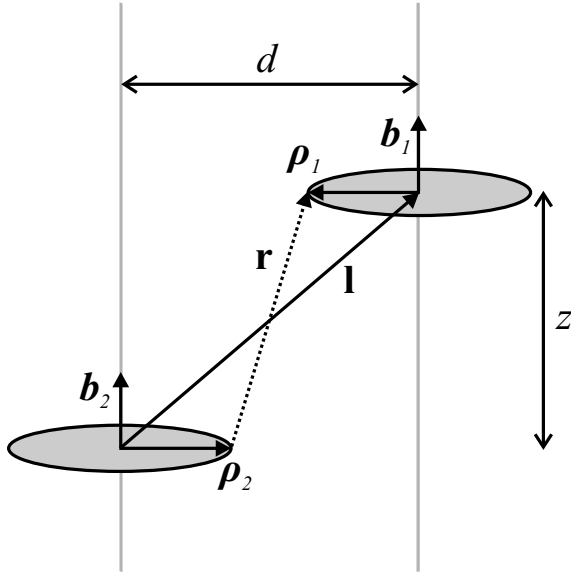


FIG. 9: Diagram illustrating the notations used in equation (14) and equation (19).

Noting that

$$\begin{aligned} \int_0^{2\pi} d\phi_1 \int_0^{2\pi} d\phi_2 (\rho_1 \cdot \rho_2) (\rho_1 \cdot \mathbf{l}) (\rho_2 \cdot \mathbf{l}) &= A_1 A_2 l^2 \sin^2 \theta \\ \int_0^{2\pi} d\phi_1 \int_0^{2\pi} d\phi_2 (\rho_1 \cdot \mathbf{l})^2 (\rho_2 \cdot \mathbf{l})^2 &= A_1 A_2 l^2 \sin^4 \theta \\ \int_0^{2\pi} d\phi_1 \int_0^{2\pi} d\phi_2 (\rho_1 \cdot \rho_2)^2 &= 2A_1 A_2, \end{aligned} \quad (17)$$

where $A_1 = \pi \rho_1^2$ and $A_2 = \pi \rho_2^2$ are the respective areas of the loops, we find

$$\begin{aligned} U &= \frac{\mu b_1 b_2}{4\pi(1-\nu)} \frac{A_1 A_2}{l^3} (8 - 24 \sin^2 \theta + 15 \sin^4 \theta) \\ &= -\frac{\mu b_1 b_2}{4\pi(1-\nu)} \frac{A_1 A_2}{l^3} (1 + 6 \cos^2 \theta - 15 \cos^4 \theta). \end{aligned} \quad (18)$$

The expression for the energy of interaction between two circular loops (18) was derived by Foreman and Eshelby⁵⁷ using the isotropic elasticity approximation, and reported in the literature by Barnes⁵⁸. The form of this equation is similar to that of equation (12). In both cases the energy varies as a function of distance between the defects as $U \sim l^{-3}$. We also see that the product of the Burgers vector and the area of the loop plays the part of the effective formation volume. Unsurprisingly, the characteristic scale of interaction energies (a fraction of an electronvolt) is similar in both cases. For practical calculations, it is convenient to express formula (18) in terms of two variables, the distance d between the glide cylinders of the loops, and the distance z between the habit planes of the

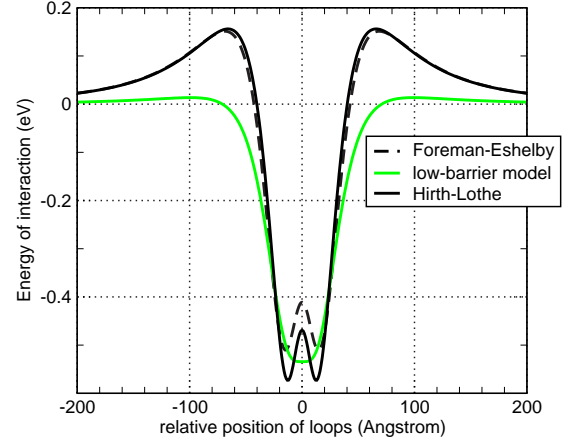


FIG. 10: Energy of interaction between two circular ($R = 9.4\text{\AA}$) self-interstitial $\mathbf{b} = a/2\langle 111 \rangle$ dislocation loops in iron evaluated using the 'exact' isotropic elasticity expression (14), the Foreman-Eshelby expression (18), and the 'low barrier model' (20), where the curve describing interaction between the loops as a function z exhibits low potential barriers for reaction between the loops. The elasticity calculations were performed assuming $\nu = 0.29$ and $\mu = 82 \cdot 10^9$ Pa.

loops. In terms of these variables, equation (18) can be written in the form

$$U(z, d) = -\frac{\mu b_1 b_2}{4\pi(1-\nu)} \frac{A_1 A_2}{(z^2 + d^2)^{3/2}} \times \left[1 + \frac{6z^2}{(z^2 + d^2)} - \frac{15z^4}{(z^2 + d^2)^2} \right]. \quad (19)$$

Our analysis of experimental data on the statistics of migration of dislocation loops suggests that the Foreman-Eshelby expression (18) overestimates, at least for the case of the $\mathbf{b} = a/2\langle 111 \rangle$ loops considered here, the height of potential barriers for reaction between the loops. The fact that equations (14) and (18) for the energy of interaction between the loops may not be accurate is not surprising since, for example, it is known that even at room temperature iron is elastically anisotropic⁷⁻⁹. Hence the isotropic elasticity formulae (14), (18) should be treated as estimates for the strength of interaction as well as for the functional form for the law of interaction between the loops. The use of the isotropic elasticity approximation (where the energy of interaction between the loops depends only on the relative orientation of the Burgers vectors of the loops and the relative positions of the loops, and is independent of the orientation of the Burgers vector of the loop relative to the crystal lattice) has the advantage that the functional form for the energy of interaction between the loops is sufficiently simple, to

enable fast evaluation of terms in the right-hand side of equations (9). The elastic anisotropy approximation does not change the general functional form for the energy of interaction between the loops, which at large distances between the loops varies as (distance) $^{-3}$, but it introduces an element of complexity in the angular dependence of the energy of interaction, as was shown for the full anisotropic elasticity case by Willis⁵⁹.

In this study, together with the original Foreman-Eshelby expression (18), we also use an alternative form, motivated by experiment, for the energy of interaction (the ‘low-barrier model’), which we derive from equation (18) by modifying some of its numerical coefficients

$$U(z, d) = -\frac{\mu b_1 b_2}{4\pi(1-\nu)} \frac{A_1 A_2}{(z^2 + d^2)^{3/2}} \times \frac{13}{10} \left[1 + \frac{1}{4} \frac{6z^2}{(z^2 + d^2)} - \frac{1}{4} \frac{15z^4}{(z^2 + d^2)^2} \right]. \quad (20)$$

A curve calculated using equation (20) is shown in Figure 10 together with the curves evaluated using equations (14) and (18). Equation (20), where the energy of interaction between the loops is independent of the orientation of their Burgers vectors with respect to the crystal lattice, still refers to the isotropic elasticity approximation.

We note that the inclusion of anisotropic elasticity effects does not alter the general functional form of the laws describing interaction between the defects. Since in this work we focus on the generic new features of Brownian motion of defects associated with the fact that defects interact, we do not specifically investigate the role played by the anisotropic elasticity effects.

In the next two sections of the paper we apply the Langevin dynamics method to the treatment of migration of two and three interacting loops, and also investigate Brownian motion of an individual loop interacting with statistically distributed vacancy clusters.

VI. CORRELATED BROWNIAN MOTION OF NANO-DISLOCATION LOOPS

In this section we focus attention on solving equations (9) and on investigating the part played by the interaction between migrating nano-dislocation loops. We find that the interaction between migrating loops, and between loops and vacancy clusters, acting as pinning centres for the loops, gives rise to striking deviations in the statistics of motion of loops from the statistics of ‘free’ Brownian motion investigated in the past by MD simulations^{10,11,14–17} and analyzed using interaction-free Langevin dynamics equations^{12,36,37,43}. Also, the Langevin dynamics simulations described below use the effective values of diffusion coefficients, derived from experimental observations for freely migrating loops, which take into account the presence of intrinsic impurities.

We start by considering the case of two interacting $\mathbf{b} = (a/2)\langle 111 \rangle$ loops of diameters $d_1 = 16\text{nm}$ and $d_2 =$

15nm migrating in nominally pure iron at $T_0 = 650\text{K}$. The diffusion coefficients for the loops, derived from the values measured for a single loop, and scaled using the inverse perimeter length law (6) are $D_1 = 296\text{nm}^2\text{s}^{-1}$ and $D_2 = 315\text{nm}^2\text{s}^{-1}$. The glide cylinders of the loop are separated by the distance $l = 37\text{nm}$. Using the Foreman-Eshelby expression (18), we see that the scale of elastic interaction between the loops in this case (the depth of the potential well similar to that shown in Figure 10) is of the order of -3eV . After taking into account the possible weakening of interaction due to elastic anisotropy effects, we conclude that the binding energy, holding the two loops together, is of the order of $E_b \sim 2\text{eV}$. Given that $\exp(-E_b/k_B T_0) \sim 3 \cdot 10^{-16}$, it is not surprising to see that in experiment the loops stay together, migrating as two bound entities over a long period of time, exceeding the entire duration of experimental observation $\sim 80\text{s}$. Figure 11 illustrates this behaviour, showing the trajectories of the loops simulated by integrating the coupled Langevin equations, and comparing them with trajectories observed experimentally using *in-situ* electron microscopy. In simulations and in observations we find a fairly similar scale of fluctuations for the position of the centre of mass of the loops. Simulations also confirm that the strength of elastic interaction is sufficient for holding the loops together as bound entities over the entire interval of time spanned by the simulation ($\sim 20\text{s}$). Figure 12 shows simulated trajectories of loops whose size and initial positions are similar to that observed using *in-situ* electron microscopy and shown in Figure 1. This case is more interesting and complex. The loop seen on the right (R) is sufficiently far apart from the loop in the centre (C), and the binding energy between these two loops, evaluated using the Foreman-Eshelby formula (18), is of the order of 0.06eV . Simulations show, in agreement with experiment, that this loop (R) is very weakly bound to the other two, and is able to move almost freely. We clearly see this trend already in the series of snapshots in Figure 1, and now this observation is confirmed directly by simulation. We see that the trajectory of loop R remains in the vicinity of the other two loops for no longer than 50s , and then loop R gets detached from the other two, and continues performing effectively free Brownian motion until the end of the time interval spanned by the simulation.

On the other hand, the scale of elastic interactions binding loops L and C together is of the order of 0.3eV , which is significantly greater than the energy of binding for loops C and R. Figure 12 shows that not only is this energy sufficient for capturing loop L, which comes in the field of view of the microscope from a distant part of the specimen, and appears only in the third snapshot shown in Figure 1, but it is also sufficiently strong for binding the loops together over the entire interval of simulation spanning 200s . It may appear surprising that a binding energy as low as 0.3eV can actually hold the two migrating loops together over such a long interval of time. Indeed the Arrhenius exponential factor for $T_0 = 675\text{K}$

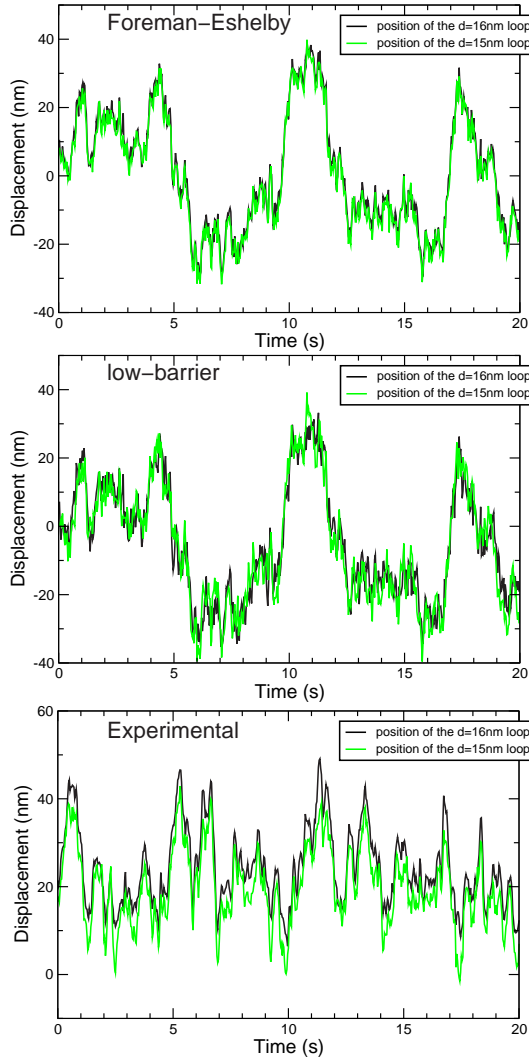


FIG. 11: Comparison of trajectories of motion for two interacting $d = 16\text{nm}$ and $d = 15\text{nm}$ prismatic $\mathbf{b} = a/2\langle 111 \rangle$ dislocation loops migrating in pure iron at $T = 650\text{K}$. The glide cylinders of the loops are 37 nm apart. The top figure shows the trajectories of the two loops simulated using the Foreman-Eshelby expression (18) for the energy of interaction between the loops. The trajectories shown in the middle were simulated using equation (20). The figure at the bottom shows the trajectories of the loops observed experimentally using *in-situ* electron microscopy.

and $E_b = 0.3\text{ eV}$ is just $\exp(-E_b/k_B T) \approx 10^{-3}$, and the transition state theory^{60,61} would predict that the two loops should break apart on the nano-second timescale. However, in the present case the pre-factor derived from a transition state theory treatment^{60,61} does not apply, and instead the rate of escape by diffusion from a potential well is given by⁶²

$$\dot{r} \sim \frac{D}{W^2} \exp(-E_b/k_B T), \quad (21)$$

where D is the effective diffusion coefficient, and W is the width of the potential well, which in the case of elastic

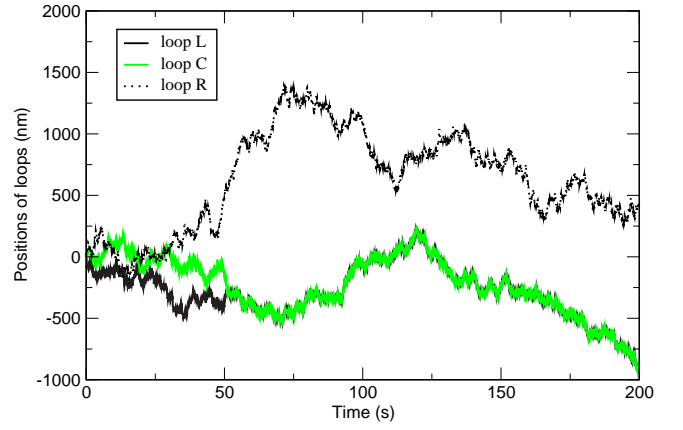


FIG. 12: Simulated trajectories of Brownian motion for the three interacting dislocation loops shown in Figure 1. Indexes L, C and R refer to the loops seen in Figure 1 on the left, in the centre, and on the right. The trajectories were simulated using the coupled Langevin equations of motion for the loops (9) assuming that the energy of interaction between the loops is given by formula (20). Simulations were performed for $T_0 = 675\text{K}$.

interaction is of the same order of magnitude as the effective size of interacting dislocation loops. For $D \sim 10^3\text{ nm}^2\text{s}^{-1}$ and $W \sim 10\text{ nm}$, we find that the probability of the system of two bound loops falling apart per unit time equals $\dot{r} \sim 5.7 \cdot 10^{-2}\text{ s}^{-1}$. In other words, the two loops bound by the relatively weak elastic forces are able to stay together as a single entity for up to $\sim 100\text{ s}$. A direct simulation extending over a much longer interval of time shows that for the case of three interacting loops illustrated in Figure 12 the bound state of the two loops L and C remains stable on the timescale of $\sim 1000\text{ s}$, after which the loops separate. This relatively long timescale of stability does not contradict our initial estimate based on equation (21), since a direct Langevin simulation takes into account the effect of the shape of the potential well on the escape probability, not taken into account in formula (21) derived for the case of a square well⁶².

To quantify the argument given above we consider a set of coupled Langevin equations for the two migrating and interacting loops

$$\begin{aligned} \frac{dz_1}{dt} &= -\frac{D_1}{k_B T} \frac{\partial U(|z_1 - z_2|)}{\partial z_1} + \sqrt{2D_1}\xi_1(t), \\ \frac{dz_2}{dt} &= -\frac{D_2}{k_B T} \frac{\partial U(|z_1 - z_2|)}{\partial z_2} + \sqrt{2D_2}\xi_2(t). \end{aligned} \quad (22)$$

Introducing new independent variables $z = z_1 - z_2$ and $Z = (D_2 z_1 + D_1 z_2)/(D_2 + D_1)$, we transform equations (22) as

$$\begin{aligned} \frac{dz}{dt} &= -\frac{(D_1 + D_2)}{k_B T} \frac{\partial U(|z|)}{\partial z} + \sqrt{2(D_1 + D_2)}\xi_z(t), \\ \frac{dZ}{dt} &= \sqrt{2\frac{D_1 D_2}{D_1 + D_2}}\xi_Z(t), \end{aligned} \quad (23)$$

where both $\xi_z(t)$ and $\xi_Z(t)$ are random δ -correlated functions of time t , i.e. $\xi_z(t)\xi_z(t') = \delta(t - t')$ and $\xi_Z(t)\xi_Z(t') = \delta(t - t')$. According to the second of the two equations (23), the motion of the effective diffusion-weighted ‘centre of mass’ of the loops $Z(t)$ can be separated from the relative motion of the loops, described by their relative coordinate $z(t)$. This shows that the correlated motion of loops seen in Figs. 11 and 12 is the effect of trapping of loops by the attractive elastic interaction between the loops, which occurs in the moving frame of the effective diffusion-weighted centre of mass for the system of two loops.

The position $Z(t)$ of the effective diffusion-weighted centre of mass of the system of two loops, on the other hand, performs free Brownian motion entirely unaffected by the interaction between the loops. The diffusion coefficient for the position of the diffusion-weighted centre of mass $Z(t)$, according to the second of the two equations (23), is $D_1 D_2 / (D_1 + D_2)$. We note an interesting fact that this diffusion coefficient, in the limit where one of the diffusion coefficients D_1 or D_2 is significantly smaller than the other, equals the smaller of the two, irrespective of the strength of interaction between the loops. This conclusion appears to be general, for example Brownian motion of a large ensemble of interacting defects is controlled by the slowest moving particle in the ensemble.

The loops can eventually separate from each other according to equation (21), but the timescale on which this separation occurs is fairly macroscopic. This conclusion agrees with experimental observations shown in Figure 1, and many other observations of similar kind, which all exhibit extended intervals of correlated motion of loops. The fact that the loops become trapped and remain effectively immobile with respect to each other over long periods of time, is significant, since this facilitates reactions between the loops, for example the coalescence of loops, or the formation of extended rafts of loops, also observed experimentally¹⁻⁶.

In this section we showed that the relatively weak elastic interactions between migrating nano-dislocation loops are able to facilitate the formation of bound long-lived configurations, where loops are trapped together and remain effectively stationary in the moving ‘centre of mass’ frame. The formation of these quasi-stable configurations increases the probability of reaction between the loops and provides a significant driving force for microstructural evolution, particularly in the limit of high irradiation dose rate.

VII. TRAPPING OF MIGRATING LOOPS BY VACANCY CLUSTERS

In the previous sections we investigated the effect of trapping of two, or several (see Fig. 1), migrating dislocation loops by their mutual elastic fields, which occurs in the moving frame of the ‘centre of mass’ of the loops. In this section we investigate a similar effect, observed

for ion-beam irradiation conditions⁴⁻⁶, where migrating dislocation loops are trapped, in the laboratory frame, by immobile vacancy clusters.

The assertion that trapping of migrating self-interstitial loops occurs as a result of interaction between a loop and vacancy clusters situated in the glide cylinder of the loop is at this point a hypothesis, stimulated by the observation that trajectories of motion of loops formed in electron- and ion-irradiated iron are very different (see Figures 2 and 3). If a vacancy, or a vacancy cluster, approaches a self-interstitial loop in the vicinity of its perimeter, the resulting annihilation reaction gives rise to the loop changing its shape, and the vacancy cluster disappearing. Similarly, the (repulsive) interaction between a loop and a vacancy cluster situated outside the glide cylinder for the loop does not explain trapping, since the trajectories of migrating loops investigated for this case by Hudson *et al.*²⁸ resemble those shown in Figure 2. The fairly long (up to 10 s) timescales characterizing trapping of defects found in observations, are difficult to explain using the conventional transition state theory argument^{60,61} that applies to processes occurring at atomic scale. Indeed, assuming an attempt frequency of $\nu^* \sim 10^{13}$ Hz, for $T_0 = 675$ K we find that the binding energy required for trapping a loop at a lattice site for $\tau^* \sim 10$ s is of the order of $E_b \sim k_B T_0 \ln(\tau^* \nu^*) \approx 2$ eV. This fairly high energy, comparable with the formation energy for a vacancy in iron, could in principle be attributed to interaction with complex stable configurations involving carbon or nitrogen impurities⁶³. Even after noting the slightly different levels of purity of the electron- and ion-irradiated samples, this still does not explain why these stable impurity complexes only form under ion irradiation, and do not form under electron irradiation. It is probably more natural to assume that ion irradiation, producing small vacancy clusters in the core of collision cascades, generates fine vacancy cluster microstructures, interacting with, and trapping, the mobile self-interstitial dislocation loops.

The potential energy of interaction between a mobile loop and a vacancy cluster defect is shown in Figure 8. The energy scale characterizing interaction between the defects for the case shown in this Figure is less than 0.9 eV. The shape and the energy scale of curves describing elastic interaction between a dislocation loop and an immobile vacancy cluster varies, according to equation (10), as a function of the size of the loop, and the position of the vacancy cluster within the glide cylinder of the loop. Hence it is expected that a nano-scale loop migrating in a crystal containing vacancy defects would move under the action of a field of randomly distributed vacancy defects, which themselves may have randomly varying size. The fact that the location and the size of vacancy defects fluctuate causes the ‘external’ interaction potential felt by a migrating self-interstitial loop to be a fluctuating function of the position of the loop. For example, we can represent the function $U(z)$ for an individual loop, described by a single Langevin equation, by

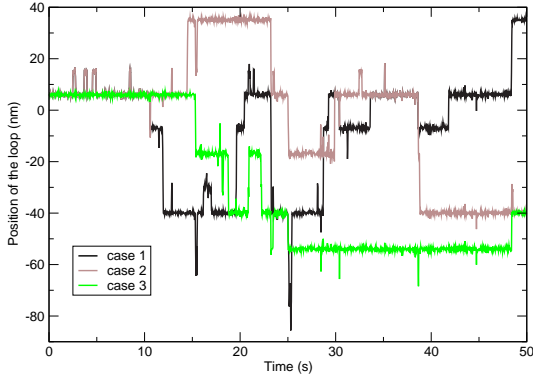


FIG. 13: Three realizations for trajectories of motion for a $d = 6\text{nm}$ prismatic $\mathbf{b} = a/2\langle 111 \rangle$ dislocation loop migrating in pure iron at $T = 675\text{K}$ and interacting with statistically distributed vacancy clusters. The diffusion coefficient for the migrating loop is $D = 1875 \text{ nm}^2\text{s}^{-1}$. The three realizations of trajectories correspond to three different realization of the potential energy landscape, corresponding to three statistical realizations of the distribution of vacancy clusters in the

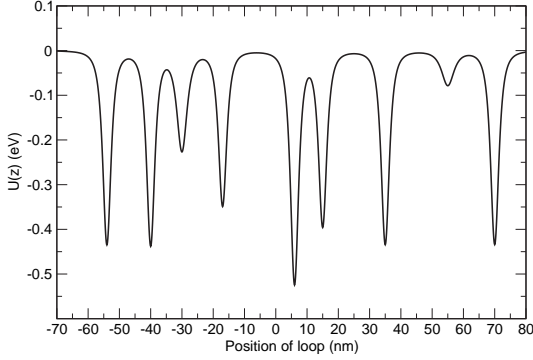


FIG. 14: The effective potential energy $U(z)$ of interaction between a mobile prismatic dislocation loop and statistically distributed vacancy clusters. The statistical realization of potential energy shown in this figure corresponds to the trajectory labeled as case 3 in Figure 13.

a set of potential wells of varying depth and width, distributed along the trajectory of migration for the loop.

Figure 13 shows three examples of trajectories of migration of a single $d = 6\text{nm}$ prismatic dislocation loop migrating in pure iron and interacting with statistically distributed vacancy clusters. The effective potential energy of interaction, corresponding to case 3 shown in Figure 13, is shown in Figure 14. The simulated trajectories of migration of the loop closely resemble those shown in Figures 3 and 15, and other similar trajectories observed earlier^{4,6,41}. The similarity between the fairly characteristic shape of trajectories found in simulations and in experimental observations, and the similarity between the timescales characterizing the trapping events, suggest that it is the elastic interaction between the loops and vacancy clusters formed under cascade irradiation that

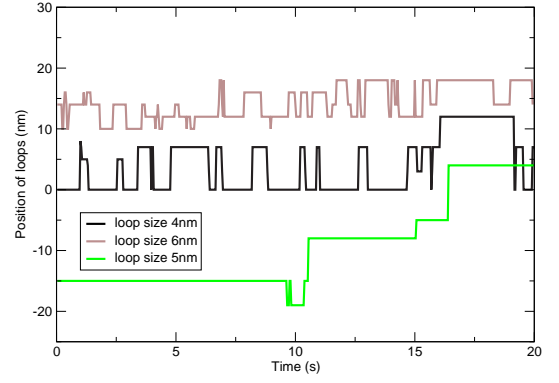


FIG. 15: Examples of experimentally observed trajectories of migration for prismatic $a/2\langle 111 \rangle$ dislocation loops of various size in pure iron irradiated with 150 keV Fe^+ ions to a dose of $\sim 0.65 \text{ dpa}$. The temperature of the specimen is 673K.

likely gives rise to the unusual statistics of motion (hopping) of loops observed by *in-situ* electron microscopy for ion-irradiated materials. Such vacancy clusters remain almost invisible in electron microscope images⁴¹. The statistics of trapping and de-trapping events, and transitions between the trapping sites seen in Figure 13 is in good agreement with the estimated residence times given by equation (21). We therefore conclude that it is the combined effect of elastic interaction between the loops and the vacancy clusters, and Brownian migration of the loops, that is likely responsible for the unusual features of migration of loops in ion-irradiated iron shown in Figures 3 and 15. Effects associated with elastic long-range interaction between migrating loops themselves are responsible for the correlated motion of loops frequently observed in high-energy electron irradiated iron, which is shown in Figure 1.

VIII. CONCLUSIONS

In this paper we developed a Langevin dynamics model and showed that the model is able to match real-time *in-situ* electron microscope observations of dynamics of migration and interaction between mobile nano-scale defects. We find that diffusion of defects combined with effects of elastic interactions gives rise to the occurrence of new modes of microstructural evolution, involving defect trapping and correlated motion of defects, which in turn strongly influence the rates of reaction and coalescence between the defects. The Langevin dynamics approach described above is able to model the dynamics of motion of radiation defects on realistic timescales (10 to 1000 s), matching those of experimental observations, as opposed to MD simulations that are only able to address timescales many orders of magnitude shorter.

The Langevin dynamics model appears particularly suitable for treating the effects of interaction between the defects, which so far have proved difficult to include in

kinetic Monte Carlo simulations, while at the same time offering advantages related to the computational implementation of the algorithm. The new method will likely prove effective for interpreting experimental data on microstructures formed by ion-beam irradiation of materials, where the high-dose rate effects and various phenomena related to long-range interactions between the defects have so far proved difficult to address using other modelling techniques and algorithms.

Acknowledgments

One of the authors (SLD) gratefully acknowledges stimulating discussions with V.V. Bulatov, and hospitality of Prof. C.H. Woo at Hong-Kong Polytechnic Uni-

versity, where part of this work was completed. This work was funded partly by the United Kingdom Engineering and Physical Sciences Research Council under grant EP/G003955 and the European Communities under the contract of Association between EURATOM and CCFE. The views and opinions expressed herein do not necessarily reflect those of the European Commission. This work was also supported by EFDA staff mobility programme. We acknowledge support from Grant-in-Aid for Scientific Research (Grant No. 21560686) and Priority Assistance for the Formation of Worldwide Renowned Centers of Research - The Global COE Program (Project: Center of Excellence for Advanced Structural and Functional Materials Design) from the Ministry of Education, Sport, Culture, Science, and Technology of Japan.

-
- ¹ K. Arakawa, M. Hatanaka, E. Kuramoto, K. Ono, and H. Mori, *Phys. Rev. Lett.* **96**, 125506 (2006).
 - ² K. Arakawa, K. Ono, M. Isshiki, K. Mimura, M. Uchikoshi, and H. Mori, *Science* **318**, 956 (2007).
 - ³ K. Arakawa, K. Ono, and H. Mori, in: *Electron Microscopy and Multiscale Modelling, EMMM-2007*, edited by A. Avilov *et al.*, AIP Conf. Proc. No. CP999 (AIP, New York, 2008) pp. 66-78.
 - ⁴ Z. Yao, M. Hernández-Mayoral, M. L. Jenkins, and M. A. Kirk, *Philos. Magazine* **88**, 2851 (2008).
 - ⁵ M. Hernández-Mayoral, Z. Yao, M. L. Jenkins, and M. A. Kirk, *Philos. Magazine* **88**, 2881 (2008).
 - ⁶ M.L. Jenkins, Z. Yao, M. Hernández-Mayoral, and M.A. Kirk, *Journ. Nucl. Mater.* **389**, 197 (2009).
 - ⁷ S.L. Dudarev, R. Bullough, P.M. Derlet, *Phys. Rev. Lett.* **100**, 135503 (2008); S.L. Dudarev, P.M. Derlet, R. Bullough, *Journ. Nucl. Mater.* **386-388**, 45 (2009).
 - ⁸ S.P. Fitzgerald, and Z. Yao, *Philos. Mag. Lett.* **89**, 581 (2009).
 - ⁹ S.P. Fitzgerald, and S.L. Dudarev, *Proc. Roy. Soc. London* **A464**, 2549 (2008); S.P. Fitzgerald, and S.L. Dudarev, *Journ. Nucl. Mater.* **386-388**, 67 (2009).
 - ¹⁰ B.D. Wirth, G.R. Odette, D. Maroudas, and G.E. Lucas, *Journ. Nucl. Mater.* **244**, 185 (1997); *ibid.* **276**, 33 (2000).
 - ¹¹ D.J. Bacon, F. Gao, and Y.N. Osetsky, *Journ. Computer-Aided Materials Design* **6**, 225 (1999).
 - ¹² S.L. Dudarev, P.M. Derlet, and C.H. Woo, *Nucl. Instr. Meth. B* **256**, 253 (2007).
 - ¹³ Y. Satoh, H. Matsui, and T. Hamaoka, *Phys. Rev. B* **77**, 094135 (2008).
 - ¹⁴ E. Kuramoto, *Journ. Nucl. Mater.* **276**, 143 (2000).
 - ¹⁵ K. Morishita, T. Diaz de la Rubia, E. Alonso, N. Sekimura, and N. Yoshida, *Journ. Nucl. Mater.* **283-287**, 753 (2000).
 - ¹⁶ J. Marian, B.D. Wirth, A. Caro, B. Sadigh, G.R. Odette, J.M. Perlado, and T. Diaz de la Rubia, *Phys. Rev.* **65**, 144102 (2002).
 - ¹⁷ Yu. N. Osetsky, D.J. Bacon, A. Serra, B.N. Singh, and S.I. Golubov, *Philos. Magazine* **83**, 61 (2003).
 - ¹⁸ C.-H. Woo, and B.N. Singh, *Philos. Magazine* **65**, 889 (1992).
 - ¹⁹ P.B. Hirsch, A. Howie, R. Nicholson, D.W. Pashley, and M.J. Whelan, *Electron Microscopy of Thin Crystals* (Krieger, Florida, 1977).
 - ²⁰ L.M. Peng, S.L. Dudarev, and M.J. Whelan, *High-Energy Electron Diffraction and Microscopy* (Oxford University Press, 2004).
 - ²¹ Y. Serruys, M.-O. Ruault, P. Trocellier, S. Miro, A. Barbu, L. Boulanger, O. Kaitasov, S. Henry, O. Leseigneur, P. Trouslard, S. Pellegrino, and S. Vaubailon, *Comptes Rendus Physique* **9**, 437 (2008).
 - ²² D. Iracane, P. Chaix, and A. Alamo, *Comptes Rendus Physique* **9**, 445 (2008).
 - ²³ A. Möslang, *Comptes Rendus Physique* **9**, 457 (2008).
 - ²⁴ D.J. Ward and S.L. Dudarev, *Materials Today* **11**, 47 (2008).
 - ²⁵ J.E. Westmoreland, J.A. Sprague, F.A. Smidt Jr., P.R. Malmberg, *Radiation Effects and Defects in Solids* **26**, 1 (1975).
 - ²⁶ J.E. Westmoreland, P.R. Malmberg, J.A. Sprague, F.A. Smidt, *Journ. Vacuum Sci. Tech.* **12**, 511 (1975).
 - ²⁷ O.W. Holland, J. Narayan, and D. Fathy, ORNL report CONF-840760-12 (1984).
 - ²⁸ T.S. Hudson, S.L. Dudarev, and A.P. Sutton, *Proc. Roy. Soc. London* **A460**, 2457 (2004).
 - ²⁹ T.S. Hudson, S.L. Dudarev, M.-J. Caturla, and A.P. Sutton, *Philos. Magazine* **85**, 661 (2005).
 - ³⁰ M. Pelfort, Y.N. Osetsky, A. Serra, *Philos. Mag. Lett.* **81**, 803 (2001).
 - ³¹ M.A. Puigvi, Y.N. Osetsky, A. Serra, *Mater. Sci. Eng. A* **365**, 101 (2004).
 - ³² T. Opplestrup, V.V. Bulatov, G.H. Gilmer, M.H. Kalos, and B. Sadigh, *Phys. Rev. Lett.* **97**, 230602 (2006).
 - ³³ E. Martinez, J. Marian, M.H. Kalos, and J.M. Perlado, *Journ. Comp. Phys.* **227**, 3804 (2008).
 - ³⁴ J. Zinn-Justin, *Quantum Field Theory and Critical Phenomena* (Clarendon Press, Oxford, 1993), Ch.4
 - ³⁵ H. Risken, *The Fokker-Planck Equation* (Springer, Berlin, 1996).
 - ³⁶ P.M. Derlet, D. Nguyen-Manh, and S.L. Dudarev, *Phys. Rev. B* **76**, 054107 (2007).
 - ³⁷ S.L. Dudarev, *Comptes Rendus Physique* **9**, 409 (2008).
 - ³⁸ T.D. de la Rubia, *Ann. Rev. Mater. Sci.* **26**, 613 (1996).
 - ³⁹ C.W. Allen, L.L. Funk, and E.A. Ryan, *Mat. Res. Soc. Symp. Proc.* **396**, 641 (1996).

- ⁴⁰ S.L. Dudarev, J.-L. Boutard, R. Lässer, M.J. Caturla, P.M. Derlet, M. Fivel, C.-C. Fu, M.Y. Lavrentiev, L. Malerba, M. Mrovec, D. Nguyen-Manh, K. Nordlund, M. Perlado, R. Schäublin, H. Van Swygenhoven, D. Terentyev, J. Wallenius, D. Weygand, F. Willaime, *Journ. Nucl. Mater.* **386-388**, 1 (2009).
- ⁴¹ M.R. Gilbert, Z. Yao, M.A. Kirk, M.L. Jenkins, and S.L. Dudarev, *Journ. Nucl. Mater.* **386-388**, 36 (2009).
- ⁴² S.L. Dudarev, and P.M. Derlet, *J. Phys.: Condens. Matter* **17**, 7097 (2005); *ibid.* **19**, 239001 (2007); P.M. Derlet and S.L. Dudarev, *Prog. Mater. Sci.* **52**, 299 (2007)
- ⁴³ S.L. Dudarev, *Journ. Nucl. Mater.* **307-311**, 881 (2002).
- ⁴⁴ S.L. Dudarev, *Philos. Mag.* **83**, 3577 (2003).
- ⁴⁵ W.T. Coffey, Y.P. Kalmykov, and J.T. Waldron, *The Langevin equation* (World Scientific, Singapore, 1996)
- ⁴⁶ M.R. Gilbert, S.L. Dudarev, P.M. Derlet, and D.G. Pettifor, *J. Phys.: Condens. Matter* **20**, 345214 (2008).
- ⁴⁷ B.U. Felderhof, *J. Phys. A: Math. Gen.* **11**, 929 (1978).
- ⁴⁸ J.M. Deutch and I. Oppenheim, *Journ. Chem. Phys.* **54**, 3547 (1971).
- ⁴⁹ T.J. Murphy and J.L. Aguirre, *Journ. Chem. Phys.* **57**, 2098 (1972).
- ⁵⁰ K.M. Hong and J. Noolandi, *Surface Science* **75**, 561 (1978)
- ⁵¹ M. Doi and S.F. Edwards, *The Theory of Polymer Dynamics* (Clarendon Press, Oxford, 1986) chapter 3, pp. 46–90
- ⁵² J. Bastecka and F. Kroupa, *Czech. J. Phys.* **B14**, 443 (1964)
- ⁵³ M. Abramowitz and I. A. Stegun, Eds., *Handbook of Mathematical Functions with Formulas, Graphs, and Mathematical Tables*, (New York: Dover Publications, 1972)
- ⁵⁴ C.K. Ong, *phys. stat. sol. b* **111**, 331 (1982)
- ⁵⁵ Y.N. Osetsky, A.G. Mikhin, A. Serra, *Philos. Mag.* **A72**, 361 (1995)
- ⁵⁶ J.P. Hirth and J. Lothe, *Theory of Dislocations*, 2nd edition (John Wiley and Sons, Inc., 1982)
- ⁵⁷ A.J.E. Foreman and J.D. Eshelby, AERE Report 4170 (Theoretical Physics Division, Atomic Energy Research Establishment, Harwell, Berkshire, England, 1962)
- ⁵⁸ R.S. Barnes, *Journ. Phys. Soc. Japan* **18**, Suppl. III, 305 (1963)
- ⁵⁹ J.R. Willis, *Quart. Journ. Mech. Appl. Math.* **18**, 419 (1965)
- ⁶⁰ G. H. Vineyard, *J. Phys. Chem. Solids* **3**, 121 (1957)
- ⁶¹ R. Landauer, J.A. Swanson, *Phys. Rev.* **121**, 1668 (1961)
- ⁶² B.U. Felderhof, *Physica A* **387**, 39 (2008)
- ⁶³ C.C. Fu and F. Willaime, *Comptes Rendus Physique* **9**, 335 (2008)